




Micromechanics of contact-bound cohesive granular materials in confined compressionManasa Bhat K. I. ^{1,*} Ryan C. Hurley,^{2,†} and Tejas G. Murthy ^{1,‡}¹*Department of Civil Engineering, Indian Institute of Science, 560012 Bangalore, India*²*Department of Mechanical Engineering, John Hopkins University, 21218 Baltimore, USA* (Received 28 September 2023; revised 6 February 2024; accepted 29 March 2024; published 21 May 2024)

The mechanical behavior of granular materials results from interparticle interactions, which are predominantly frictional. With the presence of even very small amounts of cohesion this frictional interparticle behavior significantly changes. In this study, we introduce trace amounts of cohesive binder between the intergranular contacts in a sample of quartz particles and apply one-dimensional (1D) compression loading. X-ray computed tomography is performed *in situ* during 1D compression. We make observations at three different length scales. At the macroscopic or ensemble scale, we track the evolution of the porosity, particle size and the stress-strain response during this compression. At the microstructure or interparticle scale, we compute the directional distribution of contacts and the particles. We also track the evolution of the fabric chains with continued compression. We also evaluate particle rotations, displacements, contact twist, rotation, and sliding. We show through our experiments that even a small amount of cohesion (as low as 1% by weight) significantly changes the response at multiple length scales. This interparticle cohesion suppresses the fragmentation of grains, alters force transmission and changes the structure of the ensemble.

DOI: [10.1103/PhysRevE.109.054903](https://doi.org/10.1103/PhysRevE.109.054903)**I. INTRODUCTION**

When granular geomaterials are subjected to environmental conditions such as high pressure, temperature, and salinity over long periods of time, they often acquire cohesion between particles. Such cohesive bonds are usually amorphous links of precipitates of calcites, iron oxides, alumina, organic and inorganic compounds, depending on the type of deposition of the binder [1]. Naturally occurring geomaterials such as calcareous rocks, sandstones, and gypsiferous soils contain various components, which contribute to cohesion between individual soil particles. The presence of interparticulate cohesion imparts additional rigidity to the purely particulate skeleton [2,3], which is why cohesion is often artificially introduced into granular assemblies in grouting, canal lining, in the base layer of pavements, earthen dam slopes, in prevention of sand liquefaction and for enhancing capacity of building foundations [4–7]. Extensive understanding of the ensemble mechanical response of purely frictional granular materials has emerged from elemental experiments. While treating an ensemble of particles as a continua has allowed engineering design to be based on theories of elasticity and plasticity, it is well understood that this ensemble mechanical response of granular materials results from many interparticle interactions. In other words, the ensemble response is a function of the initial configuration of particles and their consequent rearrangement with deformation. This spatial arrangement of particles in a granular ensemble is known as fabric [8].

X-ray computed tomography (XRCT), has made it possible to quantify the fabric and microstructure of granular materials, and provide deeper insights into how interparticle interactions manifest themselves at the continuum scale. Further, important microstructural features such as localization (shear bands), grain crushing, and grain rotation, which have an important influence on the continuum (or ensemble) response, have all been investigated using x-ray computed tomography [9–20]. In understanding these effects of interparticle interactions, Hall *et al.* [21], Hurley *et al.* [16,22], and Amirrahmat *et al.* [23] recently reported both kinematics and force propagation in frictional granular materials through a series of high-fidelity experiments using a combination of XRCT and three-dimensional (3D) x-ray diffraction (3D XRD). Using 3D XRD Hurley *et al.* [16] have captured diffraction patterns for each particle in the ensemble to obtain individual grain displacements, rotations, strain and stress tensors. Subsequently they have extracted intergranular forces from the stress tensors using a numerical inference technique involving force and moment equilibrium at each intergranular contact [24]. Using these intergranular force evaluations, Zhai *et al.* [25] have computed energy dissipation in granular ensembles using various energy dissipation mechanisms such as contact sliding, twisting, and rolling.

Similarly, significant understanding of the mechanical behavior of cohesive granular materials has emerged from standard continuum elemental laboratory tests and experiments [26,27]. Consequently, engineering of these materials has followed a framework wherein the presence of interparticle cohesion is treated as an additional confinement to a purely frictional granular ensemble. The microstructure of such systems has, however, remained elusive. It is well documented that the nature and magnitude of cohesion in a cohesive

*manasak@iisc.ac.in

†rhurley6@jh.edu

‡Corresponding author: tejas@iisc.ac.in

granular ensemble plays a critical role in the overall response. At the most fundamental level, the structure of cohesive frictional materials is broadly classified into contact bound, void bound, and matrix bound based on the amount and location of deposition of the binder in the ensemble [28]. Contact bound structure consists of binder localized only at the interparticle contacts; void bound structure is one in which the binder occupies the voids in between the particles; matrix bound structure features particles distributed in the matrix of binder (concrete is a typical example of such a structure).

Thus far, the microstructure of cohesive granular materials has been inferred from insightful interpretation of elemental experimental results. For example, in the case of cemented sands, it was observed that presence of interparticle cohesion (or cementation) enhances the overall strength of the material. At the continuum level, this is visualized as an expansion of the yield surface when compared to the parent sand on the Haigh-Westergaard plane in stress space [29,30]. When such cemented sands are deformed, the interparticle cohesive bonds begin to break, and frictional interparticle interactions are recovered (i.e., with complete breakdown of bonds) [2,29,31]. Using a combination of one-dimensional compression and split tensile Brazilian tests, Leroueil and Vaughan [32] have observed progressive degradation of bonds as loading progresses in cohesive granular materials. Further, Cuccovillo and Coop [31] showed that at very large strains after complete breakage of bonds, the normal compression lines of cohesive sands either merge or run parallel to the compression line of parent sand. The central idea that has emerged from these continuum level elemental experiments on cohesive granular materials is that when a cohesive granular ensemble is sheared, there is a progressive degradation of bonds, followed by interparticle interactions, and with further loading there is a possibility of particle crushing that is reminiscent of purely frictional granular materials. Discrete element method (DEM) simulations have also been able to support the fundamental idea of progressive microstructural evolution and this basic premise has led to accurately simulating ensemble level responses of cohesive granular materials [33–36].

While most of these microstructures and their evolution have been explained through appropriate interpretation of continuum level experiments, in the recent past, direct *in situ* observations at the particle level have been possible. Zhai *et al.* [37] performed one-dimensional compression experiments with the combination of XRCT and 3D XRD on lightly cemented granular materials and reported that the presence of binder between the particles reduced the overall particle fragmentation and significantly restrained particle motion. Singh and Murthy [20] performed a set of unconfined compression tests on sands cohered with Portland cement to evaluate changes in fabric and evolution of localized deformation zones using XRCT analysis. They observed localized deformation regions where damage propagates and forms bifurcation zones in the specimen as the loading progresses. Further, Singh *et al.* [18] proposed a mesoscale entity called “fabric chains”, analogous to force chains, which are preferential pathways along the maximally aligned contact directions.

In this experimental study, we present the results of a series of experiments examining the mechanical response of lightly cemented and uncemented granular systems in confined

one-dimensional loading performed with *in situ* high-resolution synchrotron based x-ray microtomography. We further probe how small amounts of interparticle cohesion influence the response at the particle scale and how these particle scale interactions feature at the ensemble scale.

II. EXPERIMENT

A. Materials and specimen preparation

We carry out a series of one-dimensional compression experiments on uncemented and contact bound cemented granular materials. Single-crystal angular quartz particles are confined in an aluminum cylinder and compressed between steel pins in this experiment. The angular quartz particles are obtained by ball milling hydrothermally grown single-crystal α -quartz particles (Sawyer Technical Materials, LLC). The frictional (or cohesionless) samples are prepared by pouring approximately 2000 sieved particles into an aluminum cylinder with inner diameter of 1.80 mm and height of 3.6 mm to obtain an ensemble with initial packing fraction (ϕ) of 0.58. This cylinder is placed on a bottom platen of 1.8 mm diameter.

Particles ranging from 150 μm to 180 μm are mixed with fast curing epoxy with three different binder contents, i.e., 1%, 2%, and 3% epoxy by weight of the quartz particles, in order to introduce interparticle cohesion. We ensure that the interparticle cohesion is small enough such that the cohesive bonds form only at the contacts between the particles. Similarly, the cohesive samples are prepared by premixing the cohesive binder and the particles. The premixed samples are deposited in aluminium cylinders to obtain cohesive ensembles with initial packing fraction (ϕ) close to 0.64 and are cured for 24 h under compression load of 1 N at room temperature. During sample preparation, cemented and uncemented samples are all prepared at the same target density to achieve similar initial packing states. However, in the case of cemented samples, the presence of epoxy bond coating on the quartz particles facilitates the formation of a denser sample ($\phi = 0.64$) as compared to uncemented counterpart ($\phi = 0.58$). The aluminium cylinders are prelubricated with a lubricant spray before sample insertion to reduce the frictional effects between the wall and the sample. We ensure free axial motion and rotation of the entire sample by gently sliding it back and forth inside the aluminium tube using the steel platens. We also observe that the strain is uniform throughout the sample for a given loading stage. The confined samples are uniaxially compressed in the Rotation and Axial Motion Stage (RAMS) at Cornell High Energy Synchrotron Source (CHESS) beam line FAST 3A. The RAMS includes a linear actuator and a load cell for force measurements. The sensitivity of the load cell is approximately $\pm 2N$. A detailed schematic of the experimental setup is shown in Fig. 1(a).

B. Sample loading

The samples are subjected to loading in stages and XRCT imaging is carried out between every loading stage. The purely frictional granular sample is loaded in five stages and cohesive granular samples are loaded in seven stages to reach a compression load of 70 N. The samples are loaded in displacement control mode by lowering the top steel platen

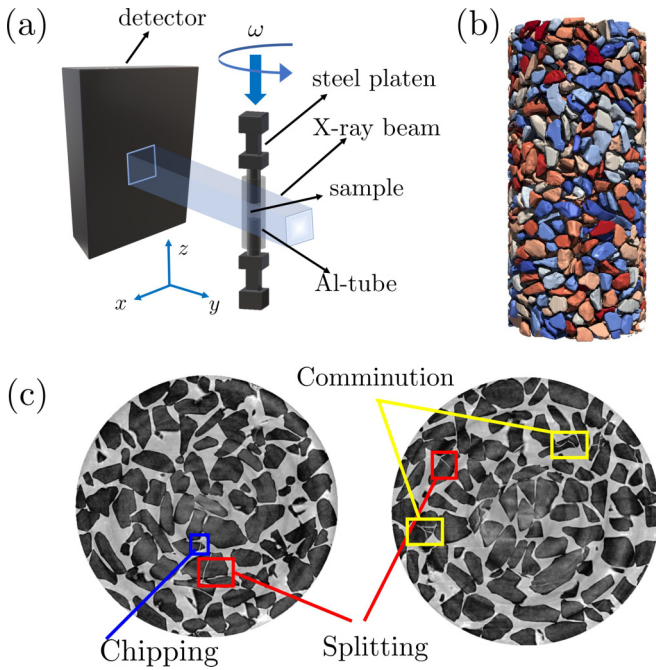


FIG. 1. (a) Schematic of the experimental setup. (b) 3D visualization of segmented specimen. (c) Cross sections from the 3D structure indicating the presence of breakage of particles in the form of splitting, chipping, and fragmentation.

into the sample until a desired load level is recorded on the load cell. The response of the cylindrical samples to one-dimensional compressive loading is presented in Fig. 2 where the vertical displacements are measured by locating the relative positions of top and bottom platens from the reconstructions of XRCT.

C. XRCT measurements and analysis

The samples are illuminated with a 87.6 keV x-ray beam 1.8 mm wide and 1.2 mm high. At each stage, the sample

is rotated through 0–180° while radiographs are captured by a camera imaging a scintillator at each 0.1° of rotation. The attenuation coefficients captured on the detector are reconstructed with a resolution of $(1.48)^3 \mu\text{m}^3$ per voxel at each load step. Details of the segmentation algorithm are presented in the Supplemental Material [38]. Features such as centroids, volumes, equivalent diameters, axes of orientation of particles are computed from the analyzed 3D structure. The visualization of segmented 3D specimen and cross-section images from the 3D structure are shown in Fig. 1(b) and Fig. 1(c), respectively.

The segmented tomography images are used to study the microstructure of the ensemble in addition to computing parameters such as coordination number, porosity, evolution of grain size distribution, and the spatial arrangement of particles, contacts, and voids. Individual particles are tracked at each stage of loading using a discrete digital volume correlation (d-DVC) algorithm [45]. A discrete-DVC algorithm works similar to classic image correlation approach of Ref. [46], but by treating each segmented grain as a correlation window. Displacements and rotations of individual grains are computed from DVC analysis.

III. RESULTS AND DISCUSSIONS

The response of cemented and uncemented granular samples in confined uniaxial compression are compared in this section. We present the results at two length scales, the structure at the ensemble scale, and the particle and contact kinematics at the microstructural scale. Lastly, we also highlight the evolution of mesoscale structures during compression.

A. Ensemble level descriptors

We present the equivalent diameter of particles computed from segmented 3D data in a cumulative density function (CDF) plot. CDFs for uncemented and cemented samples are shown in Fig. 3. The mean equivalent diameter for all the

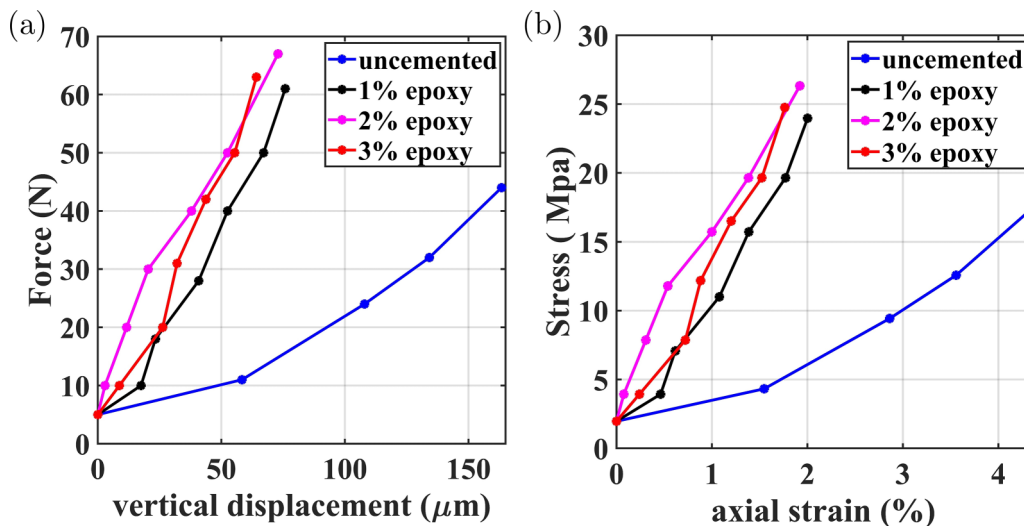


FIG. 2. (a) Force versus vertical displacement curve. Here, the vertical displacement of the entire sample is calculated from changes in the sample height (distance from the top platen to the bottom platen). (b) Corresponding stress-axial strain curve.

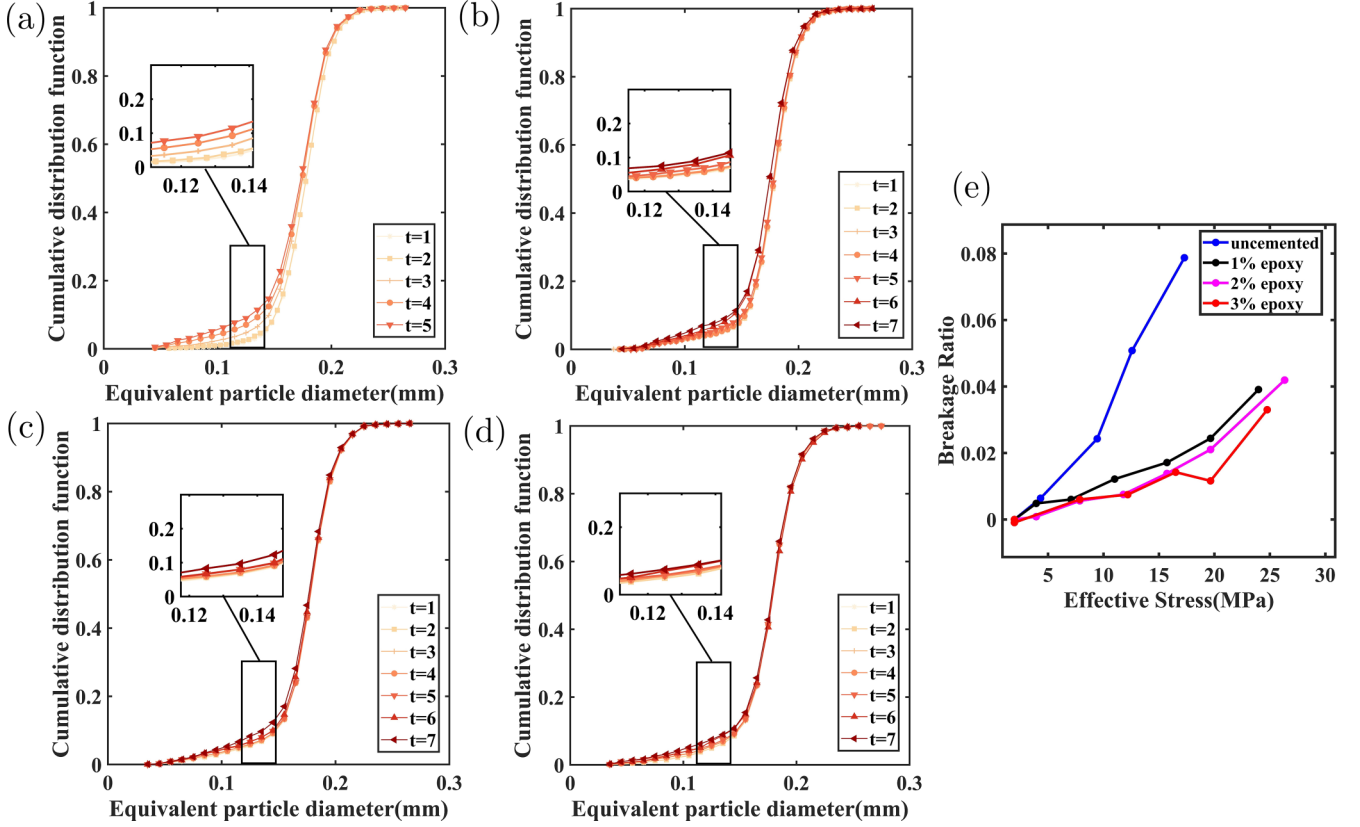


FIG. 3. Evolution of grain size distribution as loading progresses for (a) uncemented sample, (b) cemented (1% epoxy), (c) cemented (2% epoxy), and (d) cemented sample (3% epoxy). (e) Evolution of breakage of particles given by breakage ratio as the loading progresses for cemented and uncemented samples.

samples are in the range of $175 \mu\text{m}$ to $177 \mu\text{m}$. The grain size distribution curve shifts towards the left as loading progresses, indicating an increase in the cumulative density of particles with smaller particle diameter; in other words, a continuous breakage of particles occurs with increase in loading. Breakage of particles with loading is also evident from the visual examination of the grayscale images and the number of particles segmented during different loading stages. Particle breakage involves either chipping, splitting, or comminution as shown in Fig. 1(c).

We further quantify this breakage using a parameter called relative breakage [47,48]. Relative breakage measures the relative distance between the current grain size distribution from the initial and ultimate grain size distribution. In our experiment, a fractal distribution with a fractal dimension of 2.6 is used to calculate ultimate grain size distribution [49–51]. The relative breakage is computed by,

$$B_p = \int_{d_m}^{d_M} [F_u(d) - F_0(d)] d \log_{10}(d), \quad (1)$$

$$B_t = \int_{d_m}^{d_M} [F(d) - F_0(d)] d \log_{10}(d), \quad (2)$$

$$B_r = \frac{B_t}{B_p}, \quad (3)$$

where $F_u(d)$ is the ultimate grain size distribution, $F_0(d)$ is the initial grain size distribution, $F(d)$ is the current grain size

distribution, d_m is the smallest grain size, and d_M is the largest grain size. Relative breakage, B_r , is the ratio of total breakage to the breakage potential as shown in Eq. (3).

During fragmentation, larger particles are cushioned by smaller ones, preventing further crushing of the larger particles. Eventually, a fractal distribution is achieved where the morphology of the particles eliminates further stress concentrations [49]. As seen in Fig. 1(c) and Fig. 3, we observe that there is no significant change in size of largest particle, which is consistent with breakage mechanics theory [48]. Figure 3(e) shows the relative breakage ratio for cemented and uncemented samples at different stages of loading. Particles in the uncemented ensemble exhibit a relative breakage ratio of about 0.08, whereas cemented particles show a relative breakage ratio less than 0.02 at the same sample stress level and a relative breakage ratio close to 0.04 at the final stage of loading. De Bono and McDowell [36] studied one-dimensional compression on cemented sand using DEM and reported that the distribution of binder in the contact network influences the crushing of particles. From the breakage ratio plot in Fig. 3(e) we observe that the presence of even small amounts of cohesion between the grains clearly suppresses the fragmentation of particles.

The evolution of the average coordination number and packing fraction at different loading stages is shown in Fig. 4. The uncemented sample is prepared with a packing fraction of 0.58 (porosity 42%), and the cemented samples are prepared with uniform packing fractions close to 0.64 (porosity 36%).

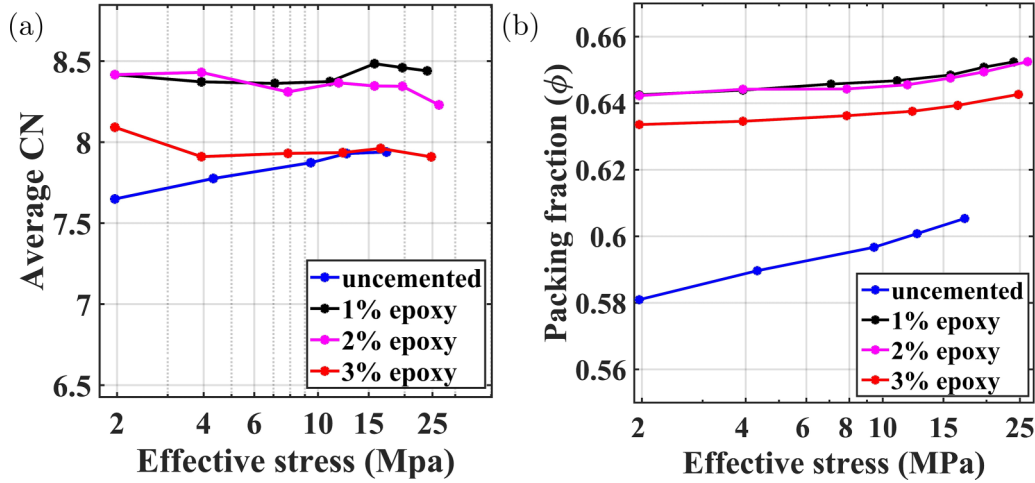


FIG. 4. Evolution of (a) average internal co-ordination number and (b) packing fraction as the loading progresses.

While direct comparison of changes in the state of packing in cemented and uncemented ensembles is not possible due to variations in the initial porosity, we observe an increasing trend in packing fraction for all the samples. Since our experiments were confined compression tests, the presence of binder between the particles in cemented samples restricts rearrangement of particles and the overall reduction in the volume (porosity) is small. On the other hand, uncemented particles undergo significant breakage and the smaller fragments fill up the voids, leading to a dramatic increase in packing fraction.

In uncemented samples, the average coordination number slightly increases from 7.6 to 7.9 with loading, predominantly due to breakage of particles. A number of small fragments fill the voids and surround the larger particles, due to which the coordination number of larger particles increases; however, these smaller fragments have lower coordination numbers, keeping the average coordination number somewhat constant. Cemented samples exhibit an average coordination number close to 8.4, which does not change significantly during loading. We compute the average coordination number using only internal particles.

B. Microstructure of cemented and uncemented grains in confined compression

Fabric is perhaps the most insightful and widely used microstructural descriptor of a granular ensemble. It is often used as a descriptor of contacts between particles, however, it is equally well applicable to the arrangement of particles, voids, and contacts in a granular ensemble. Fabric is a measure of distribution of orientation of microstructural entities and is defined by a tensor, which is referred to as a fabric tensor [8,44,52]. Recently, Singh and Murthy [20] have proposed an alternative description to quantify the orientation of entities, using principal component analysis (PCA) for quantifying fabric. They have further shown an equivalence between the covariance matrix of the contact entities and the contact normal fabric tensor. Using this equivalence, the fabric tensor (F)

for a granular ensemble is given by:

$$Cov = \begin{bmatrix} \bar{n}_1 & \bar{n}_2 & \dots & \bar{n}_p \end{bmatrix} \begin{bmatrix} \bar{n}_1^T \\ \bar{n}_2^T \\ \vdots \\ \bar{n}_p^T \end{bmatrix} = \sum_{i=1}^{N_p} \bar{n}_i \otimes \bar{n}_i, \quad (4)$$

while the fabric tensor is given by:

$$F = \frac{1}{N_p} \sum_{i=1}^{N_p} \bar{n}_i \otimes \bar{n}_i, \quad (5)$$

where N_p is the number of entities (particles or contacts), \bar{n}_i is the unit vector corresponding to direction of i th entity, and \otimes is the dyadic product.

The fabric tensor is a second-order tensor and is symmetric and positive definite with real eigenvalues and has distinct orthogonal eigenvectors for a set of normal vectors, which span a three-dimensional space. We calculate the fabric tensors for all the particles as well as contacts. After segmenting the image stack obtained from the CT scans, the principal axes of orientation of each particle and each contact are calculated and the fabric tensor for each stage of loading is computed. Fabric tensors for particles are computed as

$$F = \lambda_1[\bar{e}_1 \otimes \bar{e}_1] + \lambda_2[\bar{e}_2 \otimes \bar{e}_2] + \lambda_3[\bar{e}_3 \otimes \bar{e}_3], \quad (6)$$

where $\lambda_1, \lambda_2, \lambda_3$ represents eigenvalues and $\bar{e}_1, \bar{e}_2, \bar{e}_3$ are corresponding eigenvectors.

Fabric tensors for contacts are evaluated using Eq. (5) where N_p is number of contacts, i.e., $2N_p$ contact normal vectors, and \bar{n}_i refers to the i th contact normal vector. The minor eigenvector for a given contact is considered as its contact normal as the spread of contact points are minimum in that direction. We evaluate the fabric and contact tensors at both the particle scale and the ensemble scale.

Global fabric tensors for contact as well as particles are presented in Table I and II for uncemented and cemented samples, respectively. For these ensemble fabric tensors, the nondiagonal entries are nearly zero since major orientation

TABLE I. Global fabric tensor for contact and particle for uncemented sample in the first stage of loading.

Contact fabric	Particle fabric
$\begin{bmatrix} 0.2897 & -0.0013 & -0.0219 \\ -0.0013 & 0.3059 & -0.0126 \\ -0.0219 & -0.0126 & 0.4023 \end{bmatrix}$	$\begin{bmatrix} 0.3702 & -0.0058 & 0.0236 \\ -0.0058 & 0.3594 & 0.0187 \\ 0.0236 & 0.0187 & 0.2704 \end{bmatrix}$

direction is along the vertical axis as we deposit the particles under gravity. The diagonal components of the contact fabric tensor for an uncemented sample, in the first stage of loading are $F_{11} = 0.2897$, $F_{22} = 0.3059$, and $F_{33} = 0.4023$. The sample cemented with 2% epoxy exhibited diagonal values of $F_{11} = 0.3108$, $F_{22} = 0.3080$, and $F_{33} = 0.3812$ in the first stage of loading. The vertical normal component of contact fabric tensor, F_{33} , of both cemented and uncemented samples show that the contacts are mainly oriented in the z direction, while the particles themselves are oriented mainly in the x - y direction. Figure 5 presents the contact and fabric tensors for each particle visualized as ellipsoids. The ellipsoids are oriented along dominant eigenvectors. The samples are composed of highly angular, nonconvex quartz particles. The particles are oriented with their major axes along the x - y direction and the contacts are dominantly oriented along the vertical direction as seen in Fig. 5. Since fabric tensors provide a quantification of the overall orientation of contact normals, particles, and voids in an average sense, directional distribution of these orientations are also plotted in the form of a spherical histogram. In addition, we quantify the degree of fabric anisotropy using the second invariant of the deviatoric part of the fabric tensors for both contacts as well as particles (quantification of fabric anisotropy and directional distribution analysis are detailed in Supplemental Material [38]). Individual grain kinematics such as displacements, rotations at particle scale using the DVC algorithm are presented in the next section.

C. Characterization of grain kinematics

The mean values of grain rotations and displacements for both cemented and uncemented samples are presented in Fig. 6 and Fig. 7, respectively. The uncemented sample shows a mean rotation magnitude of 1° and the cemented samples show a smaller mean rotation of individual grains of 0.5° . Mean values of displacement for individual grains were computed from the DVC algorithm. Uncemented samples undergo about twice the grain displacements of cemented samples, as seen in Fig. 7.

TABLE II. Global fabric tensor for contact and particle for cemented sample (2% epoxy) in the first stage of loading.

Contact fabric	Particle fabric
$\begin{bmatrix} 0.3108 & -0.0026 & -0.0034 \\ -0.0026 & 0.3080 & 0.0012 \\ -0.0034 & 0.0012 & 0.3812 \end{bmatrix}$	$\begin{bmatrix} 0.3590 & 0.0028 & 0.0066 \\ 0.0028 & 0.3657 & -0.0043 \\ 0.0066 & -0.0043 & 0.2753 \end{bmatrix}$

In the case of uncemented granular materials, large magnitudes of grain displacements and rotations are observed in the initial stages of loading, indicative of rearrangement of particles as the sample loading progresses. At the macro scale, this is reflected in the changes in packing fraction (Fig. 4). The presence of a small amount of cohesive binder that adheres the particles also restricts movement of the particles, which results in significantly smaller rotations and displacements. When such cemented specimens are loaded, the cohesive interparticle contact bonds undergo progressive degradation, in other words, the cohesive bonds between the particles break, which is why some particles show large displacements and rotations, which leads to a slight increase in their mean values.

Figure 8 presents the individual grain rotations and displacements for different stages of loading for a cemented sample (2% epoxy), where the color bar shows the magnitude of rotations and displacements. The displacements are typically less than $6 \mu\text{m}$ and the incremental rotations are within 1° . In addition, Figs. 8(d) and 8(h) present the average displacements and rotations of all the particles in the ensemble as a function of normalized height, $\frac{z}{h}$ where z is the z coordinate of center of mass of the particle and h is the sample height. These plots are constructed by initially binning each grain into one of six bins that evenly divide the height of the sample at the corresponding load step and subsequently computing average displacements and rotations for particles in each bin. Since the volume correlation is performed on the 3D image stacks corresponding to two successive loading steps, $t = 1 \rightarrow 2$ refers to correlation between second and first loading stage, $t = 2 \rightarrow 3$ refers to correlation between third and second loading stage and so on. The grain rotations and displacements for uncemented sample are presented in Fig. 9. In contrast to the values of particle rotations and displacement of cemented samples, uncemented samples exhibit displacements up to $25 \mu\text{m}$ and rotations within 4° . The ends of the sample in proximity with the end platens show increased grain rotations when compared to the grains in the middle of the specimen as shown in Fig. 9(d). The magnitude of mean grain rotations and grain displacements for cemented particles are significantly less than that of uncemented counterparts. The samples are uniaxially loaded from the top for all the experiments. We observe that the top ends of the samples show higher displacement magnitudes compared to the bottom ends or the centers of the samples.

In addition, we compute axial strain values using the axial displacements from Fig. 2. The axial strain values for the uncemented sample during final stage of loading is about 4.33%, where as the axial strain values for cemented samples are 2% (1% epoxy), 1.92% (2% epoxy), and 1.76% (3% epoxy). Addition of traces of interparticle binder significantly reduces the axial strain in the assembly (for the same approximate axial stress) in a monotonic fashion with increasing binder content.

The uncemented sample and cemented samples have a slight variation in the initial packing fraction (a difference of 0.06). The changes in the initial packing fraction contribute to the reduction in overall axial strain and the relative displacements between particles as shown by Zhao *et al.* [17]. However, we observe that introducing traces of cementation produces a drastic reduction in particle rearrangement,

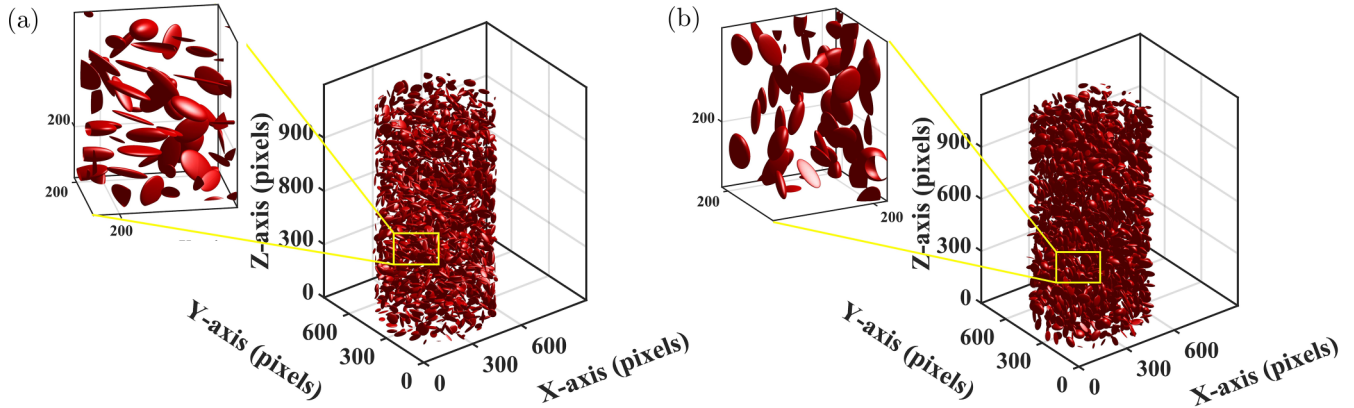


FIG. 5. (a) Fabric tensors for each particle. (b) Fabric tensors for each contact, plotted as ellipsoids oriented along their major axis of orientation for uncemented sample at fifth stage of loading.

relative movement, and axial strain. Due to relative displacement and rotations between particles, contact regions undergo deformation. The modes of deformation and some statistical measures of contact kinematics are presented in the next section.

D. Contact kinematics

We analyze three contact deformation modes from the kinematics of each pair of particles in contact: contact sliding, contact twisting, and rolling [53–55]. Interparticle contacts either slide in the direction of the plane of the contact, i.e., when the tangential force is sufficient to overcome friction, or rotate when there is relative rotation of the two grains while they remain in contact. Additionally, twisting of the contact is also possible when grains rotate around the normal to the contact. The relative displacement and relative rotation between particles on either side of a contact is used to derive the mode of deformation. The displacement and rotation for all the grains is calculated as a function of load step. We compute the axis of rotation as determined by axis-angle decomposition of a rotation matrix (detailed algorithm is provided in the Supplemental material [38]).

We compute contact parameters at each contact including the twisting and rolling of the contacts, and the contact slip (see Supplemental Material [38]). Figure 10(a), Fig. 10(b), and Fig. 10(c) show the mean values of $\Delta\theta_{\text{twist}}$, $\Delta\theta_{\text{roll}}$, and

ΔU_{slip} , respectively, across load steps, for cemented and uncemented samples. The mean values for $\Delta\theta_{\text{twist}}$ ranges between 1.2° – 2.8° , $\Delta\theta_{\text{roll}}$ ranges between 1.9° – 4.3° and ΔU_{slip} ranges from $4.7\ \mu\text{m}$ – $10.75\ \mu\text{m}$ for the uncemented sample. Cemented samples exhibit mean values of $\Delta\theta_{\text{twist}}$ of 0.4° – 0.8° , $\Delta\theta_{\text{roll}}$ ranging between 0.5° – 1.2° and ΔU_{slip} ranging from $1.6\ \mu\text{m}$ – $4.4\ \mu\text{m}$. Since the contacts are mediated in the presence of binder in cemented samples, significantly smaller relative displacements and rotations are observed.

In Fig. 11, probability density functions of these contact micromechanical entities are plotted for each load step for uncemented and cemented (2% epoxy) samples. $\Delta\theta_{\text{twist}}$, $\Delta\theta_{\text{roll}}$, and ΔU_{slip} exhibit nearly exponential distributions above the mean values and roughly power-law distributions below the mean values, for both cemented as well as uncemented samples. Zhai *et al.* [25], Radjai *et al.* [56], Mueth *et al.* [57], Blair *et al.* [58], Majmudar and Behringer [59], report an exponential distribution of interparticle forces greater than the mean force, and a power-law distribution less than the mean force in a typical uncemented granular ensemble. Zhai *et al.* [25] also report exponents from the distribution plots for the contact-micromechanical entities for purely frictional granular ensemble. Using a combination of numerical simulations and experiments, Topin *et al.* [60], Heinze *et al.* [61], Richefeu *et al.* [62] have shown that the contact stresses show an exponential decay above the mean stresses in the presence

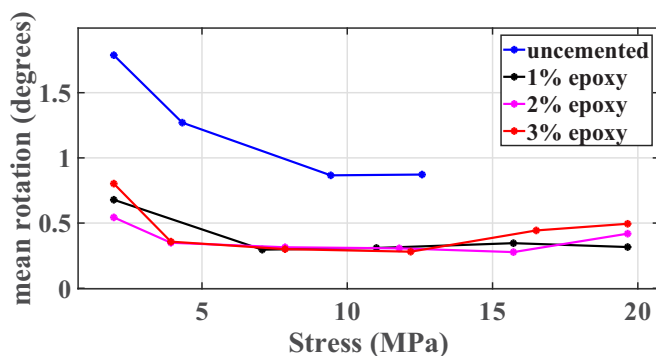


FIG. 6. Mean values of particle rotations across load steps for cemented and uncemented samples.

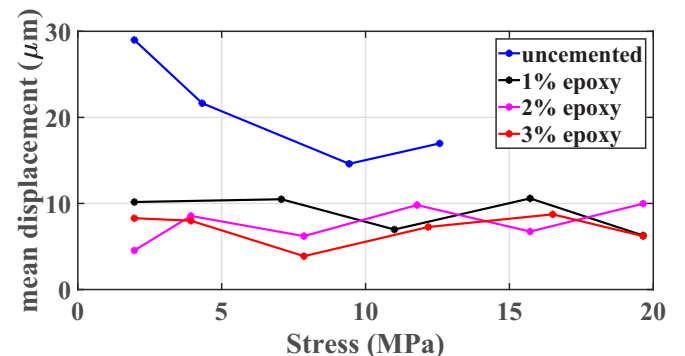


FIG. 7. Mean values of particle displacements across load steps for cemented and uncemented samples.

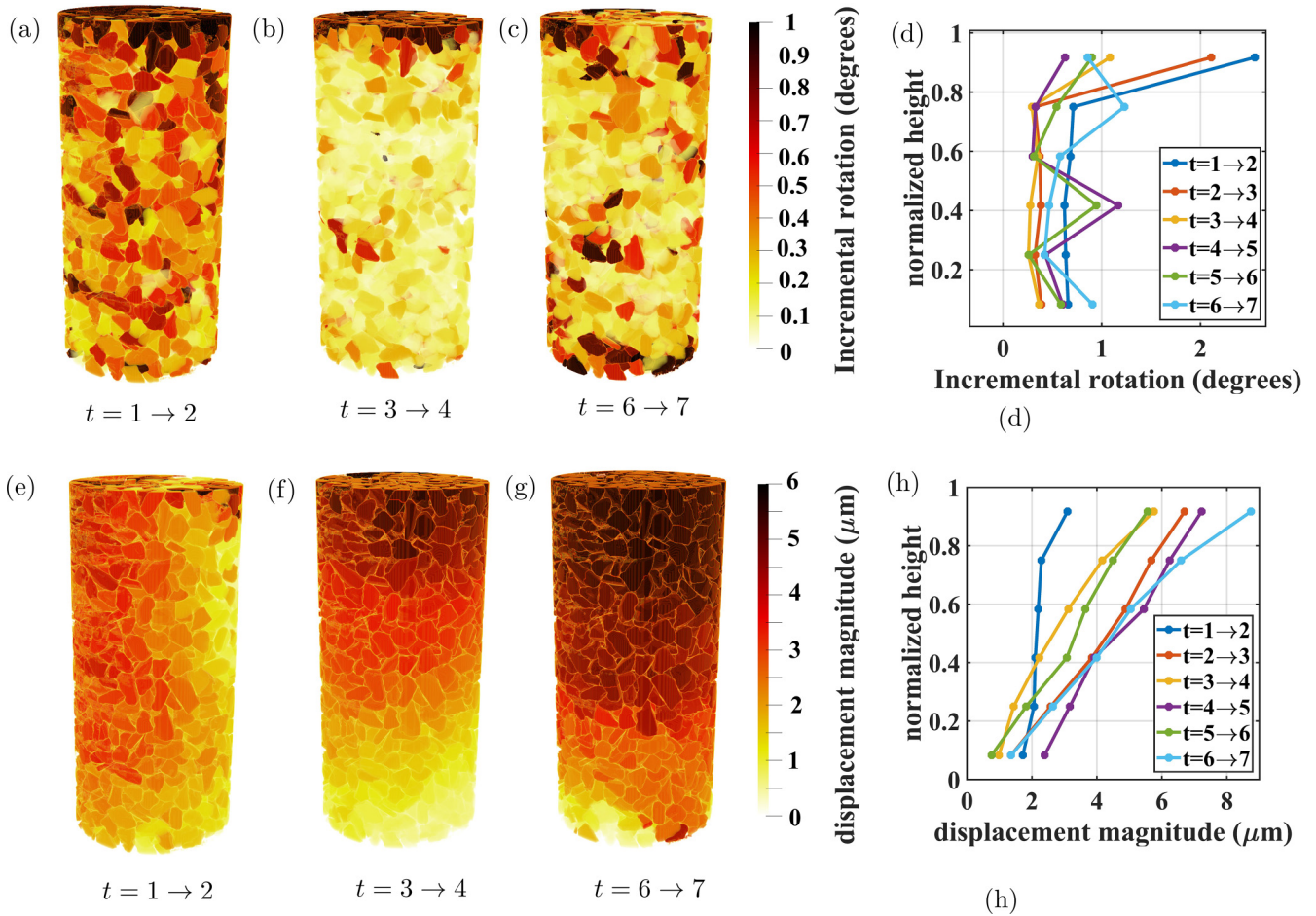


FIG. 8. Scatter plots of grain rotations and displacements. (a), (b), and (c) are magnitude of incremental grain rotations. (e), (f), and (g) are magnitude of incremental grain displacements as loading progresses for cemented sample (2% epoxy). (d) and (h) are average rotations and displacements of all particles plotted as a function of normalized height.

of cementation between particles. In the case of contact deformation modes, computing the exponents associated with the nearly exponential decay of probability density functions will help to gain useful insights into how the presence of binder in the contacts influences the overall uniformity of contact deformation. A least-squares fit of a straight line is performed on log-linear and log-log space for the distributions above and below the mean, respectively, in the probability density function plots. Subsequently, exponents are evaluated for both exponential and power-law trends and are presented in Figs. 12 and 13. The shaded region in Fig. 11 is considered for performing least-squares fit. The least-squares fit is performed using a MATLAB function polyfit to fit a polynomial of degree one. The expression used to fit a polynomial is $p(x) = p_1x + p_2$ where p_1 is the slope and p_2 is the intercept. The exponents plotted are the slopes of the least-squares fit obtained. Additional details on the computation of exponents from probability density function plots are provided in the Supplemental Material [38]. In Fig. 12, uncemented sample shows significantly higher exponent value. This higher value of exponent for the exponential tail of contact micromechanical entities indicates more heterogeneity of all such entities exceeding the mean value. A lower value of an exponent in

an exponential distribution indicates a more homogeneous specimen [22,25]. In other words, lower exponent values for cemented samples are indicative of a increased homogeneity of microstructural parameters due to the presence of binder in between the particles. Similarly, Fig. 13 represents the mean slope of the least-squares fit performed on parameters less than the mean for different loading stages for all samples. Lower relative exponents are indicative of decreased homogeneity. Power-law and exponential exponents calculated here show that lightly cemented granular samples are more homogeneous.

The three modes of contact deformation—twisting, rolling, and sliding—are known to play governing roles in mechanical failure, energy dissipation, and stress-strain behavior of granular assembly [53]. Recent findings suggest that particle breakage in granular assemblies directly dissipates only a small amount of energy but facilitates energy dissipation by enhancing grain rearrangements (due to relative motion between particles) [48,63,64]. The contact displacement caused by the relative deformation of contact points on either side of the contact plays a key role in the computation of total energy dissipated by contacts. In the recent past, few constitutive models for cohesive granular materials have incorporated

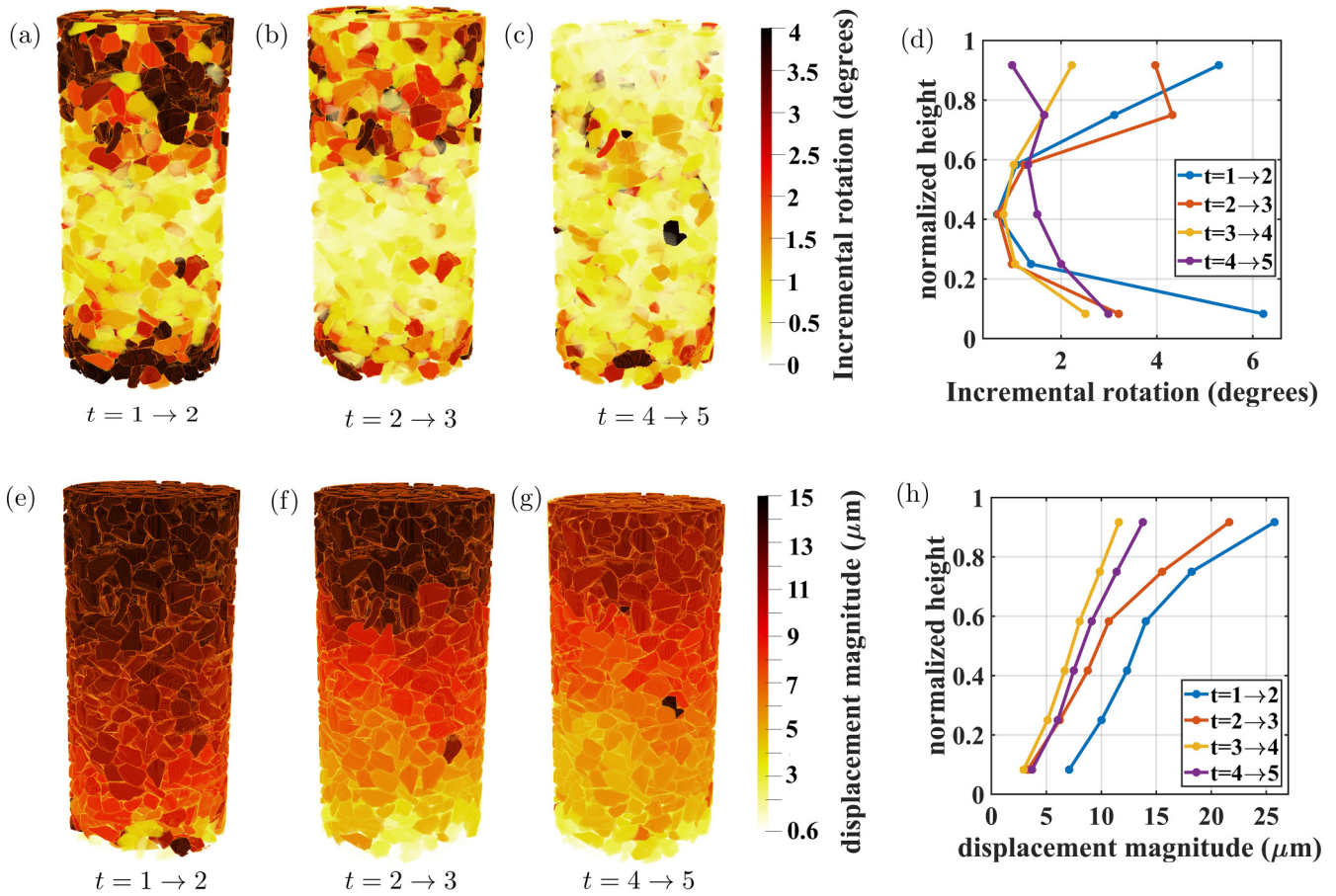


FIG. 9. Scatter plots of grain rotations and displacements. (a), (b), and (c) are magnitude of incremental grain rotations. (e), (f), and (g) are magnitude of incremental grain displacements as loading progresses for uncemented sample. (d) and (h) are average rotations and displacements of all particles plotted as a function of normalized height.

damage energy, and energy dissipation in contacts as internal state variables [48,65–67]. Hence, the observations made regarding contact micromechanical entities are insightful in extracting energy dissipation and damage energy during mechanical loading.

E. Evolution of fabric chains

In granular ensembles, force traverses the system through contacts between the particles [68]. These interparticle contacts form structural entities usually referred to as force chains. However, identifying these paths of force transmission

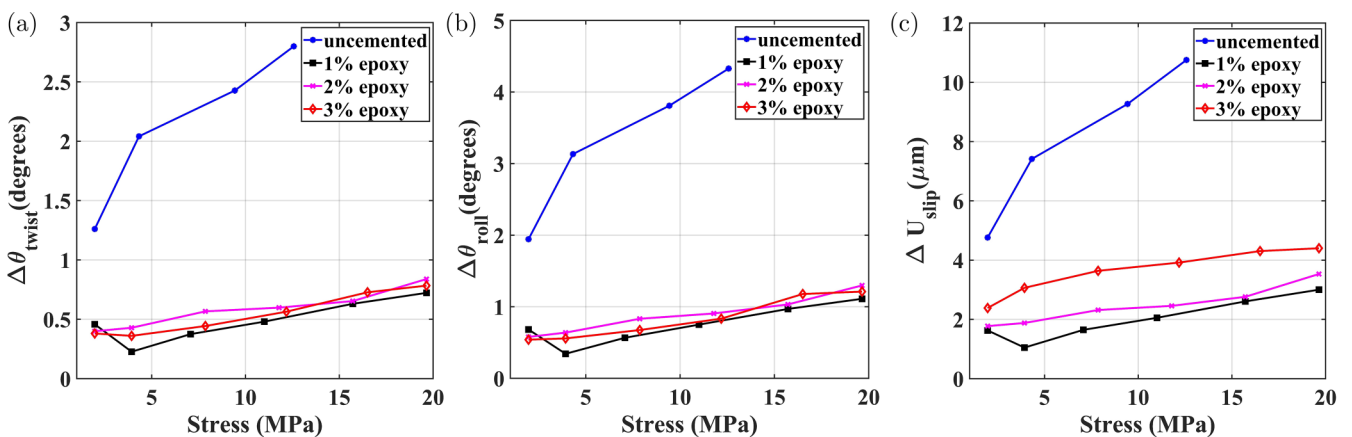


FIG. 10. (a) Mean values of $\Delta\theta_{\text{twist}}$ across load steps. (b) Mean values of $\Delta\theta_{\text{roll}}$ across load steps. (c) Mean values of ΔU_{slip} across load steps, for cemented and uncemented samples.

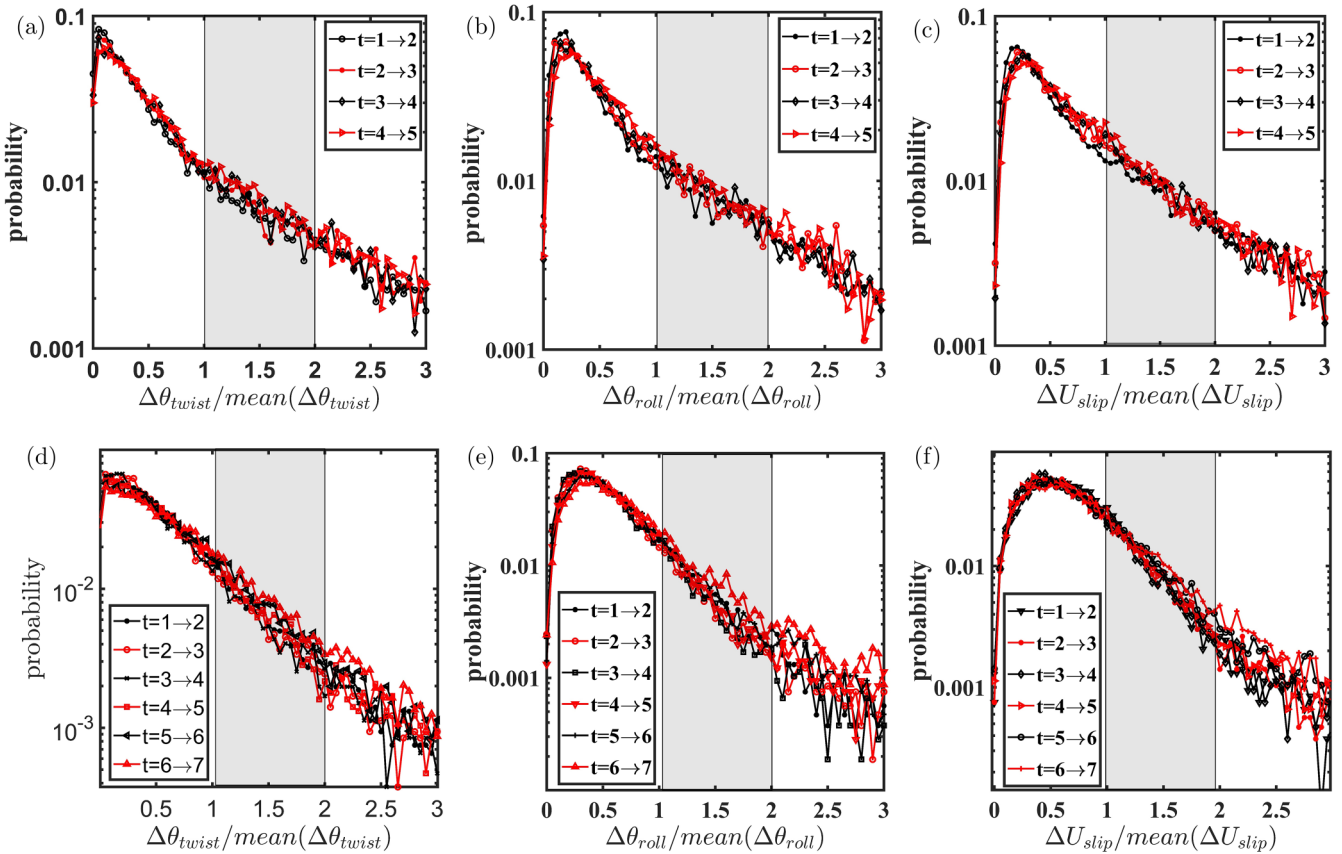


FIG. 11. Probability density functions of micromechanical contact quantities. (a), (b), and (c) are distributions of $\Delta\theta_{twist}$, $\Delta\theta_{roll}$, and ΔU_{slip} , respectively for uncemented sample. (d), (e), and (f) are distributions of $\Delta\theta_{twist}$, $\Delta\theta_{roll}$, and ΔU_{slip} , respectively for cemented sample (2% epoxy). Distributions are plotted in log-linear space to highlight the approximate exponential distributions of all quantities above their respective mean values. The shaded region reflects the region over which exponent values are extracted for further analysis.

through experiments has been possible only through photoelasticity or through a combination of 3D XRD/Xray CT [16,23,59]. In the absence of direct measurement of intergranular forces, the evolution of rearrangement of interparticle contact network provides insights about the force transmission

in the ensemble [18,69]. Fabric chains are similar structural entities, which are indicative of the path of maximally aligned contacts in a granular ensemble [18]. They can be thought of as surrogate estimates of force propagation in an assembly. Fabric chains are computed as described in the next paragraph

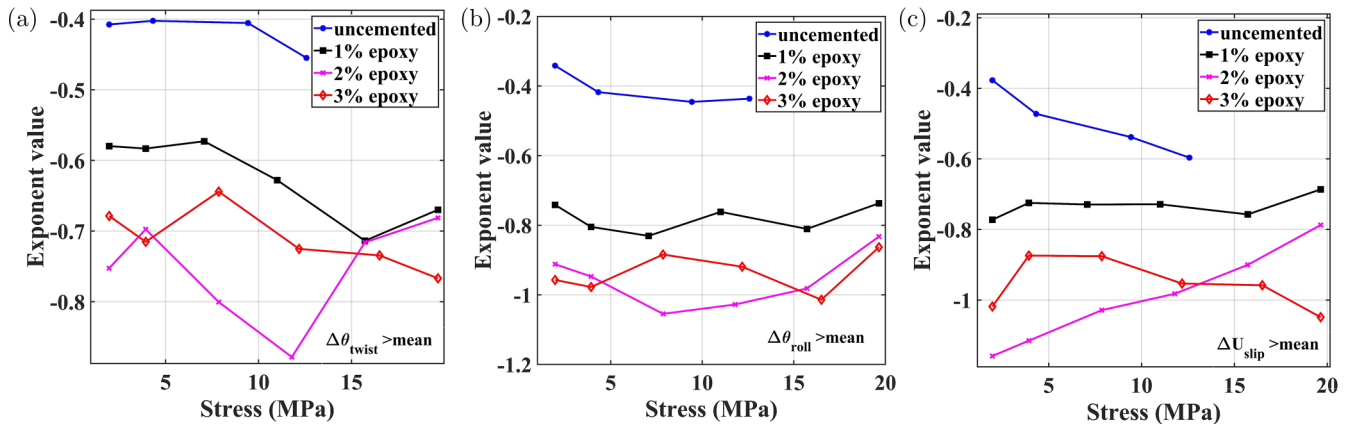


FIG. 12. Exponent values of distribution for subset of contacts for which contact micromechanical entities are greater than mean. A region of plot in log-linear space is extracted for analyzing the exponent value trends. (a), (b), and (c) are exponent values of $\Delta\theta_{twist}$, $\Delta\theta_{roll}$, and ΔU_{slip} , respectively, for uncemented and cemented samples.

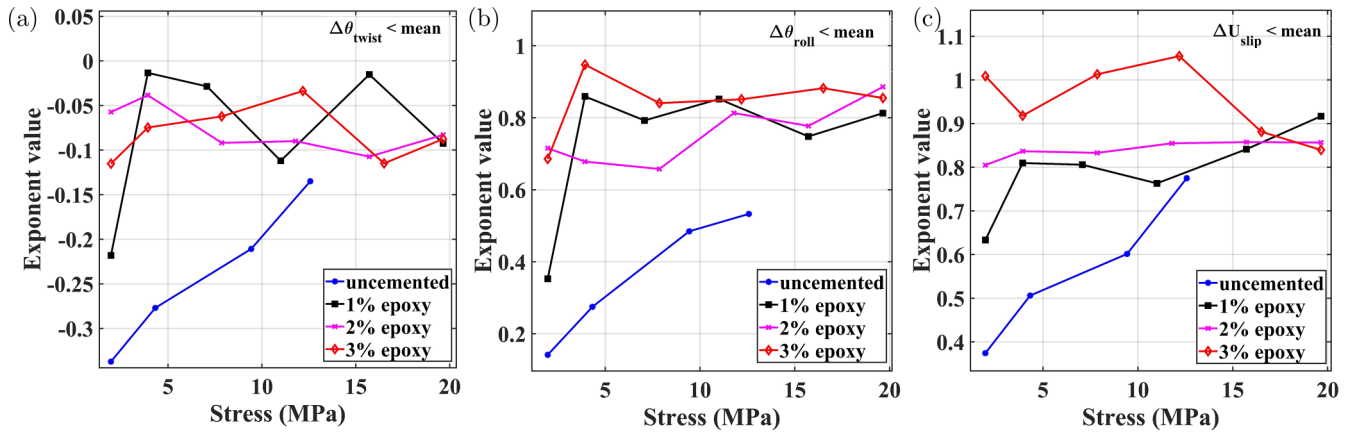


FIG. 13. Exponent values of distribution for subset of contacts for which contact micromechanical entities are lesser than mean. A region of plot in log-log space is extracted for analyzing the exponent value trends. (a), (b), and (c) are exponent values of $\Delta\theta_{twist}$, $\Delta\theta_{roll}$, and ΔU_{slip} , respectively, for uncemented and cemented samples.

and detailed algorithmically in the Supplemental Material [38].

Particles in the top layer of the cylindrical specimens are seeded for both cemented as well as uncemented samples. The particles seeded in the first stage of loading are tracked using DVC results and the same set of particles are seeded in the subsequent loading stages. For cemented samples, even though about 140 particles are seeded at the top, there are only a few unique fabric chains (about 2% of chains) percolating from the top to bottom of the specimens. Many of the fabric chains that emerge from the top merge into a few dominant chains percolating throughout the specimen, as seen in Fig. 14. These fabric chains form a webbed structure, akin to the force-chain distribution seen through DEM simulations of cemented granular system [70]. On the other hand, uncemented samples show a greater number of unique fabric chains (about 16% of chains) emerging from the top layer of

particles, which percolate through entire sample as depicted in Fig. 15.

In the cohesive granular samples, the interparticle cohesion breaks down and the number of unique fabric chains also increases, which is presented in Fig. 14. For the cemented sample with 2% epoxy, at the second stage of loading, only about 2.1% of fabric chains emerge as unique chains as seen in Fig. 14(a). As is apparent in the final stage of loading for the cemented sample (2% epoxy), about twice as many fabric chains (5% of chains) percolate through entire sample as seen in Fig. 14(c). Emergence of a larger number of unique fabric chains implies more unique pathways of transfer of force indicating that more particles are involved in force transmission. Binder disintegration at higher loading stages for cemented samples and corresponding increase in emergence of unique fabric chains is reminiscent of uncemented samples, which inherently have more unique fabric chains

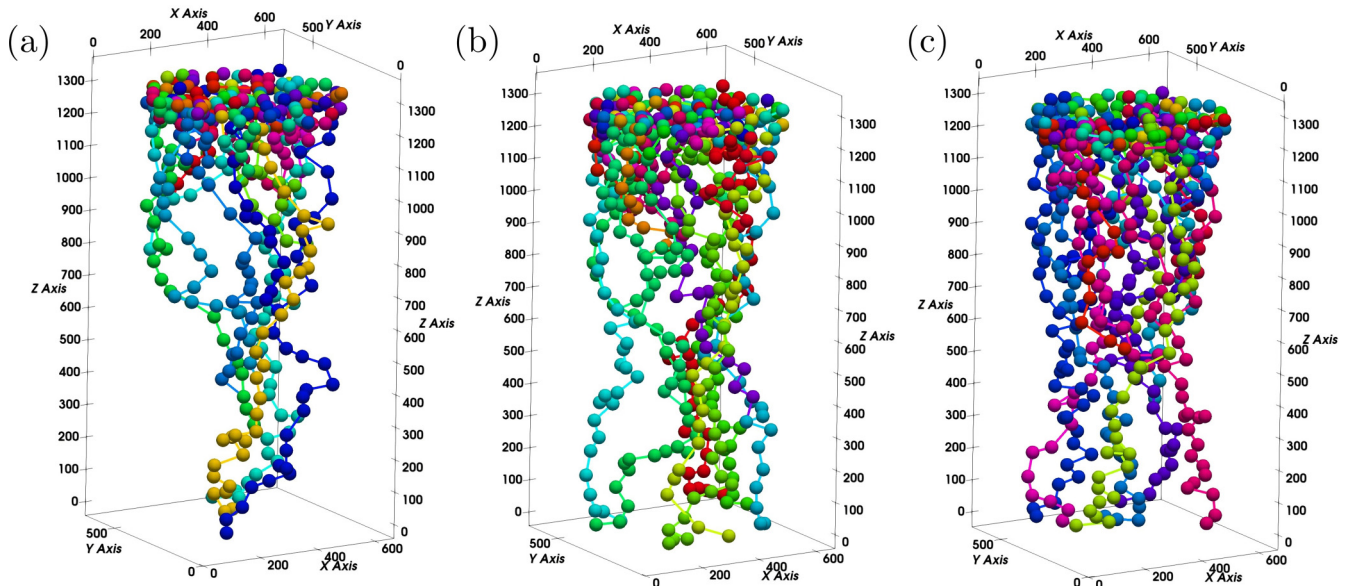


FIG. 14. (a) Fabric chains for cemented sample (2% epoxy) in the second stage of loading, when the particles present at the top layer are seeded. (b) Fabric chains for fourth stage of loading. (c) Fabric chains for seventh stage of loading.

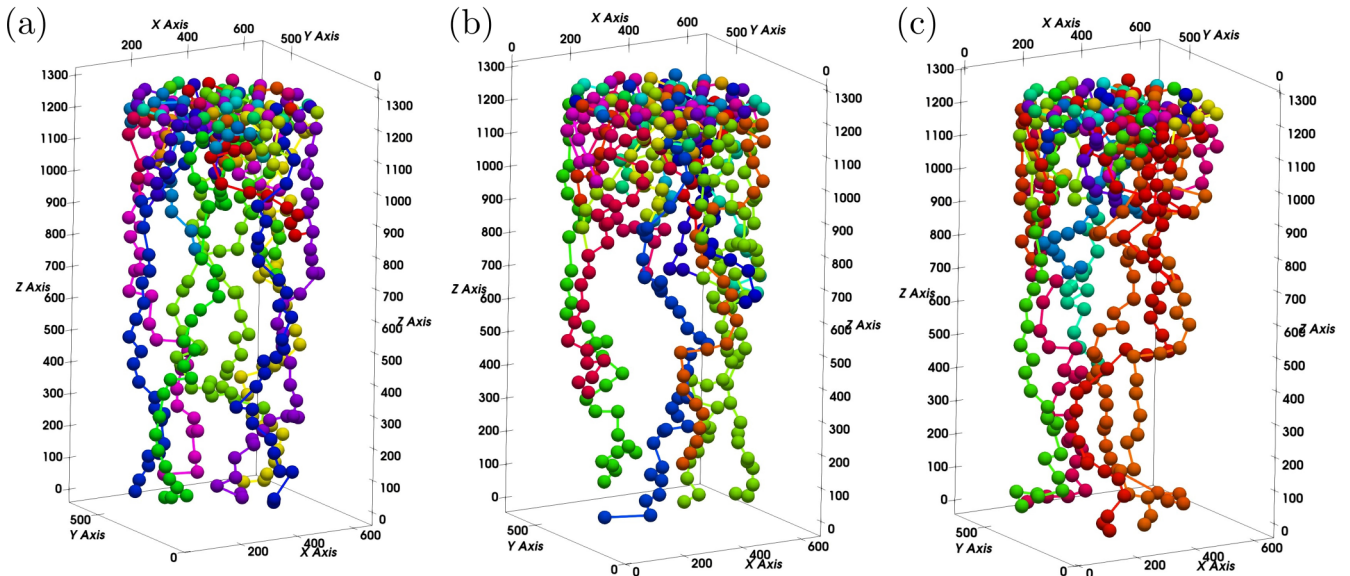


FIG. 15. (a) Fabric chains for uncemented sample in the third stage of loading, when the particles present at the top layer are seeded. (b) Fabric chains for fourth stage of loading. (c) Fabric chains for fifth stage of loading.

percolating through the system. Furthermore, we compute specific properties related to fabric chain networks to quantify the evolution of fabric chains in cemented and uncemented samples. We compute fabric chain length (number of particles per fabric chain) and tortuosity coefficient, which signifies the degree of tortuosity in fabric chains. Additionally, we define a participation index for each particle present in the fabric chain. This index quantifies the degree of involvement of each particle in the set of all fabric chains, thus indicating the extent of merging observed in these chains. A detailed analysis of the quantification of fabric chains is provided in the Supplemental Material [38].

Wang and Leung [70] conducted a series of triaxial experiments and discrete element numerical simulations on uncemented and artificially cemented materials. They report that the force chains in cemented samples exhibit a strong webbed pattern due to the presence of a cohesive network. In our study, we observe from the analysis of fabric chain characteristics that the presence of a binder network at the interparticle contacts promotes more tortuous paths for force transmission between sample boundaries than those present in the absence of cement. As a consequence, fewer chains percolate from top to bottom resulting in a webbed structure. In the recent past, Zhai *et al.* [37] used a combination of 3D XRD and XRCT to extract volume averaged intragranular stresses in a cohesive granular system and showed that there exists coaxiality of compressive granular stresses and macroscopic sample strain. They have also reported that presence of cementation suppresses particle fragmentation and kinematic measures in the ensemble. However, in our study, due to the absence of measurement of contact stresses, we use a mesoscale measure to characterize the regions and paths of maximum stiffness and report emergence of webbed chains, which arises due to presence of strong cement network in cohesive granular materials. Further, we evaluate the interplay of particle fragmentation, cement degradation, formation of new noncohesive frictional contacts, particle rearrangement,

and presence of lateral confinement in the overall macroscopic response of cohesive granular ensemble. In the absence of lateral confinement, Singh and Murthy [20] have performed XRCT studies under uniaxial compression loading and have reported emergence of segregated zones of distinct particle velocities due to localized deformations. While the absence of confinement causes bulging due to dilative volumetric response and increased porosity in the specimen, we found that with the presence of lateral confinement there is no significant localization of deformation (no shear bands are observed) and it also strongly influences the particle fragmentation phenomenon due to which the porosity continuously decreases throughout the experiment. These macroscopic observations are fundamentally governed by grain-scale processes and changes in the microstructure. Recently, few constitutive models have incorporated micromechanically inspired internal state variables, which are measurable and are capable of adequately capturing all the grain-scale processes, which occur in the ensemble [48,65,66,71]. While Tengattini *et al.* [67] have incorporated the parameters involving progressive cementation damage as an internal variable in a thermomechanics-based model, they have validated it using XRCT experiments on spherical glass beads with calcite cementation. In the past, Golchert *et al.* [72] demonstrated the possible use of findings from microtomography studies to validate DEM simulation results to assess and model the breakage of granular agglomerates. In addition, studies from Fu *et al.* [73], Wu *et al.* [74] compare results such as particle kinematics and local strains from tomography-based experiments with DEM models with one-to-one mapping of sand particles. However, these studies focused on frictional granular materials without the mediation of cohesion between the contacts. The results from our experiments have potential implications in benchmarking and validation of DEM models for granular materials in the presence of cohesive binder.

In this study, we use more realistic angular quartz particles as a granular material; the results obtained from our study

pertaining to evolution of contact micromechanics such as contact roll, twist, and slip quantities can be insightful in extracting energy dissipation and damage energy during mechanical loading. The results obtained in this research study are also insightful in building a relation between microscale phenomena and macro level responses of cohesive granular materials using homogenization schemes [66,75,76].

IV. CONCLUSIONS

The major thrust of this experimental study is to gain a comprehensive understanding of ensemble level as well as particle level response of contact-bound cohesive granular materials in confined one-dimensional loading conditions. In these experiments, we study cohesive granular materials at three different length scales: in terms of macroscopic response, in terms of the mesoscale emergence of fabric chains and the evolution of microstructural descriptors. The comparison between cemented and uncemented samples outlined in this study is also influenced by the differences in the initial packing states. The following conclusions are drawn from the analysis of the experimental observations:

(i) Evolution of grain size distribution as loading progresses and observations of the 3D internal structure indicated that particle breakage occurs in uncemented and lightly cemented samples.

(ii) The differences in fragmentation between the cemented and uncemented samples under comparable loads suggests that the presence of cement plays an important role in suppressing fragmentation at the particle scale even at very low cement fractions. Breakage analysis shows a remarkable 70% reduction in fragmentation in the presence of interparticle binder under similar stress levels.

(iii) On evaluating the fabric tensors for particles and contacts it is observed that even though the particles lie in the x - y plane, the contacts orient themselves in the direction of loading.

(iv) Characterization of grain kinematics has shown that grains in an uncemented sample experience almost twice the magnitude of axial strains, displacements, rotations, and contact roll, slip, and twist compared to cemented samples. Despite the difference in the initial packing states of the cemented and uncemented samples, which play a role in decreasing overall axial strain and displacements, the addition of small amounts of cementation causes a drastic decrease in particle rearrangement, relative movement, and axial strain.

(v) Micromechanical contact quantities such as contact slip, contact twist, and roll all exhibit roughly exponential distributions above their respective mean and power-law distribution below their mean for both cemented as well as uncemented samples. The computed relative exponent values are indicative of increased homogeneity of contact microstructural entities for cemented samples.

(vi) Analysis of mesoscale fabric chain network characteristics show that there is a webbing pattern of the chain network in cemented samples. This indicates a strong influence of the interparticle binder on the maximally aligned available stress transmission pathways.

ACKNOWLEDGMENTS

The authors acknowledge the Cornell High Energy Synchrotron Source for the beam time and thank the beam line scientist, Dr. Katherine Shanks, for assistance in the experiments. T.G.M. thanks Science and Engineering Research Board, India for funding through Grant No. SERB CRG 2022/003750.

-
- [1] D. P. Kryniene and W. R. Judd, *Principles of engineering geology and geotechnics* (McGraw-Hill, New York, 1957).
- [2] T. S. Nagaraj and B. R. Srinivasa, *Analysis and Prediction of Soil Behaviour* (Taylor & Francis, 1994).
- [3] A. Skempton and R. Northey, The sensitivity of clays, *Géotechnique* **3**, 30 (1952).
- [4] J.-M. Dupas and A. Pecker, Static and dynamic properties of sand-cement, *J. Geotech. Eng. Div.* **105**, 419 (1979).
- [5] N. Sitar, G. W. Clough, and R. C. Bachus, Behavior of weakly cemented soil slopes under static and seismic loading conditions, Technical Report (The John A. Blume Earthquake Engineering Center, Dept. of Civil Engineering; US Geological Survey, 1980).
- [6] N. S. Rad, G. W. Clough *et al.*, *The Influence of Cementation on the Static and Dynamic Behavior of Sands* (John A. Blume Earthquake Engineering Center, Stanford, 1982).
- [7] G. W. Clough, J. Iwabuchi, N. S. Rad, and T. Kuppusamy, Influence of cementation on liquefaction of sands, *J. Geotech. Eng.* **115**, 1102 (1989).
- [8] M. Oda, Initial fabrics and their relations to mechanical properties of granular material, *Soils Found.* **12**, 17 (1972).
- [9] J. Desrues, R. Chambon, M. Mokni, and F. Mazerolle, Void ratio evolution inside shear bands in triaxial sand specimens studied by computed tomography, *Géotechnique* **46**, 529 (1996).
- [10] M. Oda, T. Takemura, and M. Takahashi, Microstructure in shear band observed by microfocus x-ray computed tomography, *Géotechnique* **54**, 539 (2004).
- [11] G. Viggiani, N. Lenoir, P. Bésuelle, M. Di Michiel, S. Marelli, J. Desrues, and M. Kretschmer, X-ray microtomography for studying localized deformation in fine-grained geomaterials under triaxial compression, *Comptes Rendus Mécanique* **332**, 819 (2004).
- [12] S. A. Hall, M. Bornert, J. Desrues, Y. Pannier, N. Lenoir, G. Viggiani, and P. Bésuelle, Discrete and continuum analysis of localised deformation in sand using x-ray μ CT and volumetric digital image correlation, *Géotechnique* **60**, 315 (2010).
- [13] A. M. Druckrey, K. A. Alshibli, and R. I. Al-Raoush, 3d characterization of sand particle-to-particle contact and morphology, *Comput. Geotech.* **74**, 26 (2016).
- [14] A. Hasan and K. Alshibli, Three dimensional fabric evolution of sheared sand, *Granular Matter* **14**, 469 (2012).

- [15] M. B. Cil and K. A. Alshibli, 3D evolution of sand fracture under 1D compression, *Géotechnique* **64**, 351 (2014).
- [16] R. C. Hurley, S. A. Hall, J. E. Andrade, and J. Wright, Quantifying interparticle forces and heterogeneity in 3D granular materials, *Phys. Rev. Lett.* **117**, 098005 (2016).
- [17] B. Zhao, J. Wang, E. Andò, G. Viggiani, and M. R. Coop, Investigation of particle breakage under one-dimensional compression of sand using x-ray microtomography, *Canadian Geotech. J.* **57**, 754 (2020).
- [18] S. Singh, J. C. Miers, C. Saldana, and T. G. Murthy, Quantification of fabric in cemented granular materials, *Comput. Geotech.* **125**, 103644 (2020).
- [19] W. H. Imseeh, A. M. Druckrey, and K. A. Alshibli, 3D experimental quantification of fabric and fabric evolution of sheared granular materials using synchrotron micro-computed tomography, *Granular Matter* **20**, 24 (2018).
- [20] S. Singh and T. G. Murthy, Evolution of structure of cohesive granular ensembles in compression, *Int. J. Solids Struct.* **238**, 111359 (2022).
- [21] S. A. Hall, J. Wright, T. Pirling, E. Andò, D. J. Hughes, and G. Viggiani, Can intergranular force transmission be identified in sand? *Granular Matter* **13**, 251 (2011).
- [22] R. C. Hurley, S. A. Hall, and J. P. Wright, Multi-scale mechanics of granular solids from grain-resolved x-ray measurements, *Proc. R. Soc. Lond. A* **473**, 20170491 (2017).
- [23] S. Amirrahmat, W. H. Imseeh, K. A. Alshibli, P. Kenesei, Z. A. Jarrar, and H. Sharma, 3D experimental measurements of evolution of force chains in natural silica sand, *J. Geotech. Geoenviron. Eng.* **146**, 04020027 (2020).
- [24] R. C. Hurley, *Force Chains, Friction, and Flow: Behavior of Granular Media Across Length Scales* (California Institute of Technology, Pasadena, 2016).
- [25] C. Zhai, E. Herbold, S. Hall, and R. Hurley, Particle rotations and energy dissipation during mechanical compression of granular materials, *J. Mech. Phys. Solids* **129**, 19 (2019).
- [26] C. Mériaux and T. Triantafillou, Scaling the final deposits of dry cohesive granular columns after collapse and quasi-static fall, *Phys. Fluids* **20**, 033301 (2008).
- [27] A. Gans, A. Abramian, P.-Y. Lagrée, M. Gong, A. Sauret, O. Pouliquen, and M. Nicolas, Collapse of a cohesive granular column, *J. Fluid Mech.* **959**, A41 (2023).
- [28] G. B. Sowers and G. F. Sowers, *Introductory Soil Mechanics and Foundations* (LWW, The Netherlands, 1951), Vol. 72.
- [29] D. Airey, Triaxial testing of naturally cemented carbonate soil, *J. Geotech. Eng.* **119**, 1379 (1993).
- [30] M. Coop and J. Atkinson, The mechanics of cemented carbonate sands, *Géotechnique* **43**, 53 (1993).
- [31] T. Cuccovillo and M. Coop, Yielding and pre-failure deformation of structured sands, *Géotechnique* **47**, 491 (1997).
- [32] S. Leroueil and P. R. Vaughan, The general and congruent effects of structure in natural soils and weak rocks, *Géotechnique* **40**, 467 (1990).
- [33] M. Jiang, H.-S. Yu, and S. Leroueil, A simple and efficient approach to capturing bonding effect in naturally microstructured sands by discrete element method, *Int. J. Num. Meth. Eng.* **69**, 1158 (2007).
- [34] Y. Wang and S. Leung, Characterization of cemented sand by experimental and numerical investigations, *J. Geotech. Geoenviron. Eng.* **134**, 992 (2008).
- [35] M. Jiang, W. Zhang, Y. Sun, and S. Utili, An investigation on loose cemented granular materials via dem analyses, *Granular Matter* **15**, 65 (2013).
- [36] J. P. De Bono and G. R. McDowell, Discrete element modelling of one-dimensional compression of cemented sand, *Granular Matter* **16**, 79 (2014).
- [37] C. Zhai, D. Pagan, and R. Hurley, *In situ* x-ray tomography and 3d x-ray diffraction measurements of cemented granular materials, *JOM* **72**, 18 (2020).
- [38] See Supplemental Material at <http://link.aps.org/supplemental/10.1103/PhysRevE.109.054903> for the details of the segmentation algorithm; quantification of fabric anisotropy and directional distribution analysis; axis-angle decomposition of rotation matrix, computation of contact micromechanical parameters; computation of exponents from probability density function plots of contact micromechanical entities; detailed algorithm on computing the fabric chains; quantification of fabric chains. It also contains Refs. [39–45].
- [39] F. Alonso-Marroquin and I. Vardoulakis, Micromechanics of shear bands in granular media, *Powders and Grains*, 1st ed. (CRC Press, 2005).
- [40] M. Muthuswamy and A. Tordesillas, How do interparticle contact friction, packing density and degree of polydispersity affect force propagation in particulate assemblies? *J. Stat. Mech.: Theory Exp.* (2006) P09003.
- [41] R. P. Behringer, K. E. Daniels, T. S. Majmudar, and M. Sperl, Fluctuations, correlations and transitions in granular materials: statistical mechanics for a non-conventional system, *Philos. Trans. R. Soc. London A* **366**, 493 (2008).
- [42] A. Tordesillas and M. Muthuswamy, On the modeling of confined buckling of force chains, *J. Mech. Phys. Solids* **57**, 706 (2009).
- [43] B. Zhao and J. Wang, 3d quantitative shape analysis on form, roundness, and compactness with μ CT, *Powder Technol.* **291**, 262 (2016).
- [44] M. Oda, Fabric tensor for discontinuous geological materials, *Soils Found.* **22**, 96 (1982).
- [45] O. Stamati, E. Andò, E. Roubin, R. Cailletaud, M. Wiebicke, G. Pinzon, C. Couture, R. Hurley, R. Caulk, D. Caillerie *et al.*, Spam: software for practical analysis of materials, *J. Open Source Software* **5**, 2286 (2020).
- [46] B. D. Lucas and T. Kanade, An iterative image registration technique with an application to stereo vision, in *IJCAI'81: 7th international joint conference on Artificial intelligence* (Morgan Kaufmann Publishers Inc., San Francisco, CA, 1981), Vol. 2, pp. 674–679.
- [47] B. O. Hardin *et al.*, Crushing of soil particles, *J. Geotech. Eng.* **111**, 1177 (1985).
- [48] I. Einav, Breakage mechanics—Part I: Theory, *J. Mech. Phys. Solids* **55**, 1274 (2007).
- [49] C. Sammis, G. King, and R. Biegel, The kinematics of gouge deformation, *Pure Appl. Geophys.* **125**, 777 (1987).
- [50] G. R. McDowell and M. D. Bolton, On the micromechanics of crushable aggregates, *Géotechnique* **48**, 667 (1998).
- [51] M. R. Coop, K. K. Sorensen, T. Bodas Freitas, and G. Georgoutsos, Particle breakage during shearing of a carbonate sand, *Géotechnique* **54**, 157 (2004).

- [52] M. Oda, S. Nemat-Nasser, and M. M. Mehrabadi, A statistical study of fabric in a random assembly of spherical granules, *Int. J. Numer. Anal. Meth. Geomech.* **6**, 77 (1982).
- [53] M. R. Kuhn and K. Bagi, Contact rolling and deformation in granular media, *Int. J. Solids Struct.* **41**, 5793 (2004).
- [54] M. Jiang, Z. Shen, and J. Wang, A novel three-dimensional contact model for granulates incorporating rolling and twisting resistances, *Comput. Geotech.* **65**, 147 (2015).
- [55] Y. Wang, F. Alonso-Marroquin, and W. W. Guo, Rolling and sliding in 3-D discrete element models, *Particuology* **23**, 49 (2015).
- [56] F. Radjai, M. Jean, J.-J. Moreau, and S. Roux, Force distributions in dense two-dimensional granular systems, *Phys. Rev. Lett.* **77**, 274 (1996).
- [57] D. M. Mueth, H. M. Jaeger, and S. R. Nagel, Force distribution in a granular medium, *Phys. Rev. E* **57**, 3164 (1998).
- [58] D. L. Blair, N. W. Mueggenburg, A. H. Marshall, H. M. Jaeger, and S. R. Nagel, Force distributions in three-dimensional granular assemblies: Effects of packing order and interparticle friction, *Phys. Rev. E* **63**, 041304 (2001).
- [59] T. S. Majmudar and R. P. Behringer, Contact force measurements and stress-induced anisotropy in granular materials, *Nature (London)* **435**, 1079 (2005).
- [60] V. Topin, J.-Y. Delenne, F. Radjai, L. Brendel, and F. Mabilie, Strength and failure of cemented granular matter, *Eur. Phys. J. E* **23**, 413 (2007).
- [61] K. Heinze, X. Frank, V. Lullien-Pellerin, M. George, F. Radjai, and J.-Y. Delenne, Stress transmission in cemented bidisperse granular materials, *Phys. Rev. E* **101**, 052901 (2020).
- [62] V. Richefeu, M. S. El Youssoufi, and F. Radjai, Shear strength properties of wet granular materials, *Phys. Rev. E* **73**, 051304 (2006).
- [63] M. D. Bolton, Y. Nakata, and Y. P. Cheng, Micro-and macro-mechanical behaviour of DEM crushable materials, *Géotechnique* **58**, 471 (2008).
- [64] R. Hurley, J. Lind, D. Pagan, M. Akin, and E. Herbold, *In situ* grain fracture mechanics during uniaxial compaction of granular solids, *J. Mech. Phys. Solids* **112**, 273 (2018).
- [65] A. Das, A. Tengattini, G. D. Nguyen, G. Viggiani, S. A. Hall, and I. Einav, A thermomechanical constitutive model for cemented granular materials with quantifiable internal variables. Part II—Validation and localization analysis, *J. Mech. Phys. Solids* **70**, 382 (2014).
- [66] A. Tengattini, A. Das, G. D. Nguyen, G. Viggiani, S. A. Hall, and I. Einav, A thermomechanical constitutive model for cemented granular materials with quantifiable internal variables. Part I—Theory, *J. Mech. Phys. Solids* **70**, 281 (2014).
- [67] A. Tengattini, G. D. Nguyen, G. Viggiani, and I. Einav, Micromechanically inspired investigation of cemented granular materials: Part II—From experiments to modelling and back, *Acta Geotechnica* **18**, 57 (2023).
- [68] H. Yin and J. Dvorkin, Strength of cemented grains, *Geophys. Res. Lett.* **21**, 903 (1994).
- [69] J. Fonseca, S. Nadimi, C. Reyes-Aldasoro, M. Coop *et al.*, Image-based investigation into the primary fabric of stress-transmitting particles in sand, *Soils Found.* **56**, 818 (2016).
- [70] Y.-H. Wang and S.-C. Leung, A particulate-scale investigation of cemented sand behavior, *Canadian Geotech. J.* **45**, 29 (2008).
- [71] A. Tengattini, E. Andò, I. Einav, and G. Viggiani, Micromechanically inspired investigation of cemented granular materials: Part I—From X-ray micro tomography to measurable model variables, *Acta Geotechnica* **18**, 35 (2023).
- [72] D. Golchert, R. Moreno, M. Ghadiri, J. Litster, and R. Williams, Application of x-ray microtomography to numerical simulations of agglomerate breakage by distinct element method, *Adv. Powder Technol.* **15**, 447 (2004).
- [73] Y. Fu, L. Wang, M. T. Tumay, and Q. Li, Quantification and simulation of particle kinematics and local strains in granular materials using x-ray tomography imaging and discrete-element method, *J. Eng. Mech.* **134**, 143 (2008).
- [74] M. Wu, J. Wang, A. Russell, and Z. Cheng, DEM modelling of mini-triaxial test based on one-to-one mapping of sand particles, *Géotechnique* **71**, 714 (2021).
- [75] C. Wellmann, C. Lillie, and P. Wriggers, Homogenization of granular material modeled by a three-dimensional discrete element method, *Comput. Geotech* **35**, 394 (2008).
- [76] T. K. Nguyen, G. Combe, D. Caillerie, and J. Desrues, Investigation of a cohesive granular material: multi-scale modelling by fem-dem approach, *XVI French-Polish Colloquium of Soil and Rock Mechanics* (2013), Vol. 106.